Enhanced Intercalation Dynamics and Stability of Engineered Micro/Nano-Structured Electrode Materials: Vanadium Oxide Mesocrystals

*Evan Uchaker, Meng Gu, Nan Zhou, Yanwei Li, Chongmin Wang, and Guozhong Cao**

An additive and template free process is developed for the facile synthesis of $VO_2(B)$ mesocrystals via the solvothermal reaction of oxalic acid and vanadium pentoxide. The six-armed star architectures are composed of stacked nanosheets homoepitaxially oriented along the [100] crystallographic register with respect to one another, as confirmed by means of selected area electron diffraction and electron microscopy. It is proposed that the mesocrystal formation mechanism proceeds through classical as well as non-classical crystallization processes, and is possibly facilitated or promoted by the presence of a reducing/chelating agent. The synthesized $VO_2(B)$ mesocrystals are tested as a cathodic electrode material for lithium-ion batteries, and show good capacity at discharge rates ranging from 150–1500 mA g^{-1} and a cyclic stability of 195 mA h g^{-1} over fifty cycles. The superb electrochemical performance of the $VO_2(B)$ mesocrystals is attributed to the porous and oriented superstructure that ensures large surface area for redox reaction and short diffusion distances. The mesocrystalline structure ensures that all the surfaces are in intimate contact with the electrolyte, and that lithium-ion intercalation occurs uniformly throughout the entire electrode. The exposed (100) facets also lead to fast lithium intercalation, and the homoepitaxial stacking of nanosheets offers a strong inner-sheet binding force that leads to better accommodation of the strain induced during cycling, thus circumventing the capacity fading issues typically associated with $VO_2(B)$ electrodes.

1. Introduction

The development and implementation of nanostructured materials has led to great enhancements in Li-ion battery performance, as with many other fields.[1] The nanoscale size reduction leads to enhancements in the Li-ion battery intercalation capability by increasing the specific surface area for interfacial Faradaic reactions and the flux of Li^+ across the electrode-electrolyte interface; these effects ultimately enhance the mass and charge diffusion paths and modify the thermodynamics (compared to the bulk), which facilitates phase transitions.[2,3] Provided all the benefits of nanostructuring, the synthesis and characterization of nanostructured electrode materials of various chemistries have been extensively investigated. However, the use of nanostructures is not a panacea, and there are several performance issues, either lingering or deriving from nanostructuring, that still need to be addressed.[4] Most notably, nanostructured electrodes suffer from diminished conductivity, stability, and packing density, while at the same time exhibiting enhanced reactivity.[5–10]

The design of structurally aligned nanoparticles can circumvent the thermodynamic instability, undesired side reactions, high processing costs, and potential nano-toxicity effects associated with nanoparticle synthesis and processing.[1,11,12]

E. Uchaker, N. Zhou, Y. Li, G. Z. Cao
Department of Materials Science & Engineering
University of Washington
Seattle, WA 98195, USA
E-mail: gzcao@u.washington.edu
M. Gu, C. M. Wang
Environmental Molecular Science Laboratory
Pacific Northwest National Laboratory
902 Battelle Boulevard, Richland, WA 99352, USA

DOI: 10.1002/smll.201203187

NANO MICRO small

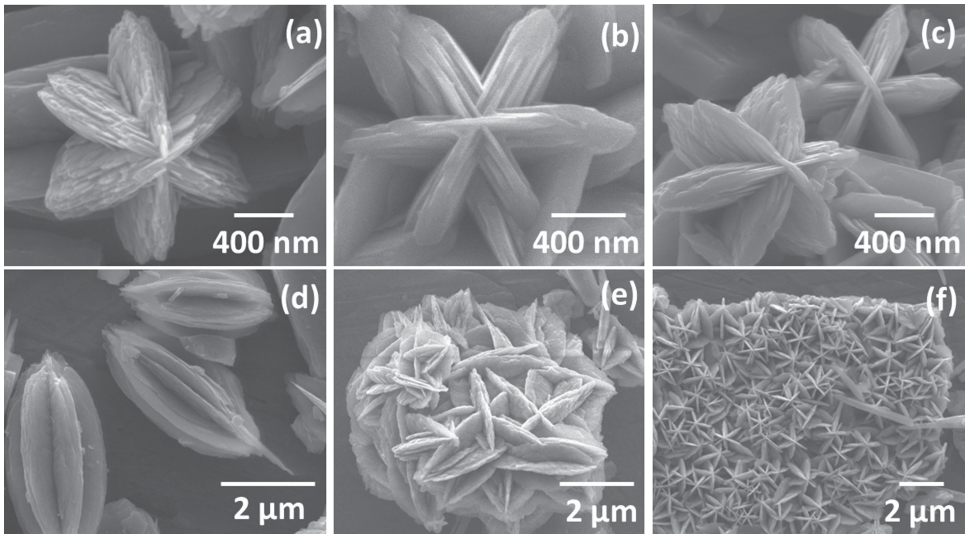

Figure 1. SEM images of the synthesized vanadium oxide mesocrystals: a–c) representative view of individual assemblies showing the stacked nanosheets composing each arm, d) longitudinal view of star-structure, and e,f) overall view of as-synthesized specimen displaying the packing density.

There has been a great deal of recent efforts in the formation and understanding of ordered nanoparticle superstructures with a vast range of architectures; in particular, crystallographically oriented nanoparticle superstructures, or mesocrystals, have been the central focus of such intrigue since described by Cölfen and Antonietti.[13–16] Until recently, mesocrystals were only studied in biomineral materials, but current research efforts have shifted towards the development of mesocrystalline organic molecules,[15,17] metal oxides,[18–21] and other functional materials.[22,23]

Novel nanoparticle arrangement has historically been achieved through the synthesis of nanocrystalline superlattices, or supercrystals, and colloidal crystals. However, individual nanoparticle orientation is not taken into account by such assemblies. Mesocrystals can be classified by their high degree of crystallinity, porosity, and subunit alignment along a crystallographic register.[14] These highly desirable properties are due in part to the mesocrystal formation mechanisms, which are still poorly understood, and make mesocrystals ideal material candidates for catalysis, sensing, and energy storage/conversion applications.[16] Mesocrystal growth often proceeds via the aggregation of precursor units, rather than the classical ion-by-ion growth mechanism, which can be attributed with the generation of crystals with hierarchical structures and complex morphologies. Several investigations of mesocrystalline $LiFePO_4$ and TiO_2 used as the electro-active material for lithium-ion battery electrodes have already been produced, but a report of mesocrystalline vanadium oxide for such an application is lacking.[20,21] Herein, we report on the solvothermal synthesis, potential formation mechanism, and electrochemical performance of VO_2(B) mesocrystals synthesized using an additive free solvothermal approach. Moreover, remarkable phase stability and excellent lithium-ion intercalation properties have been demonstrated for the obtained VO_2(B) mesocrystals.

2. Results and Discussion

VO_2(B) mesocrystals were synthesized by adopting the methods of Li et al., which involved the solvothermal reaction of V_2O_5 and oxalic acid.[24] The size and morphology of the as-prepared material was examined using scanning electron microscopy (SEM), the results of which are displayed in **Figure 1**. Figure 1a–c displays several representative individual mesocrystal assemblies, while Figure 1d–f shows an overall SEM micrograph of a typical specimen which is largely composed of uniformly micro-sized ellipsoidal star structures with an average height and width of approximately 2.8 μm and 1.5 μm, respectively. As the higher magnification images reveal, each star-structure is composed of six arms that are self-assembled from stacked nanosheets 20–60 nm thick that are radially aligned with respect to the center of the structure. Each nanosheet is intimately connected to its neighbors, resulting in a highly porous structure that should facilitate the penetration of electrolyte into the material, alleviate cycling induced strain, and decrease the lithium-ion diffusion distance. The overall thickness of each hierarchically nanostructured arm is approximately 200–300 nm.

Figure 1e,f illustrates that the star-assemblies appear to have a relatively mono-dispersed size distribution and are tightly packed, which should result in a porous and layered microstructured assembly with enhanced volumetric density and conductivity. A slight degree of variation with the morphology is apparent (Figure 1e); however, such effects are considered negligible because the arms of the structures are composed of stacked nanosheets.

Figure 2a displays the X-ray diffraction (XRD) pattern of the as synthesized material which can be indexed to the monoclinic crystalline phase of VO_2(B) (space group C2/m and JCPDS card no. 081–2392) with lattice parameters a, b, c, and β equal to 12.092 Å, 3.702 Å, 6.433 Å, and 106.6°, respectively; this analysis is consistent with literature reports.[25,26]

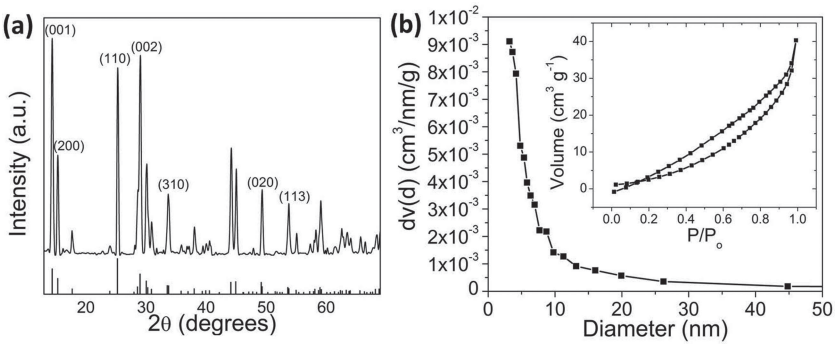

Figure 2. a) XRD spectrum and the b) BJH desorption pore size distribution for the as synthesized VO_2(B) mesocrystals (inset: N_2 adsorption–desorption isotherm).

The interlayer spacing of the phase is determined to be 6.15 Å from the (001) reflection. The sharp and high intensity diffraction peaks are indicative that the product is highly crystalline. No secondary or parasitic phases are detected, and the formation of crystalline VO_2(B) indicates that the V^{5+} ions from the original V_2O_5 precursor have been reduced to V^{4+} during the solvothermal synthesis by oxalic acid.[24,27,28]

Peak broadening analysis of the (001) XRD reflection using the Scherrer equation indicated that the average crystallite size was approximately 17 nm, substantiating the microscopy results that the VO_2(B) mesocrystals were composed of nanocrystalline subunits. The presence of the nanoparticle subunits and the porous nature of the sample were confirmed by the corresponding nitrogen sorption isotherms and Barrett–Joyner–Halenda (BJH) desorption analyses, which indicated that the majority of pores within the sample are below 15 nm (Figure 2b). The Brunauer-Emmett-Teller (BET) derived surface area was determined to be 28.4 m^2 g^{-1}, which is a reasonable value given the overall microscale of the synthesized assemblies. The amply-sized pores can provide excellent channels and cavities for complete and homogeneous Li^+ diffusion and intercalation throughout the material. Some residual chelating agent synthesized during the reaction may remain on or between the surfaces of the VO_2(B) nanosheets, and similar incorporations have been known to decrease the overall porosity of mesocrystals.[29]

Transmission electron microscopy (TEM) was then performed on a single star-assembly cross section that was prepared using an ultramicrotome, as displayed in **Figure 3**a. The cross sectioned image reveals that each arm of the star-assembly is separate from the others, indicating that the structure is not truly single crystalline. Figure 3b presents the vertex of two arms, as identified by the highlighted region in Figure 3a, and confirms the superstructure arms are composed of stacked nanosheets. A thinner ultramicrotomed specimen would have made the nanosheet stacking more pronounced; however, specimens cut to thicknesses of 60 and 80 nm continually shifted when exposed to the electron gun, most likely due to heating effects with the epoxy resin (or residual organic matter existing between the nanosheets) when cut so thin. The nanosheets measure several tens of nanometers as observed with TEM, supporting the SEM and XRD findings of the mesocrystalline primary nanoparticle size.

Selected-area electron diffraction (SAED) can be used to demonstrate the single crystalline behavior of mesocrystals due to the subunit nanoparticle alignment

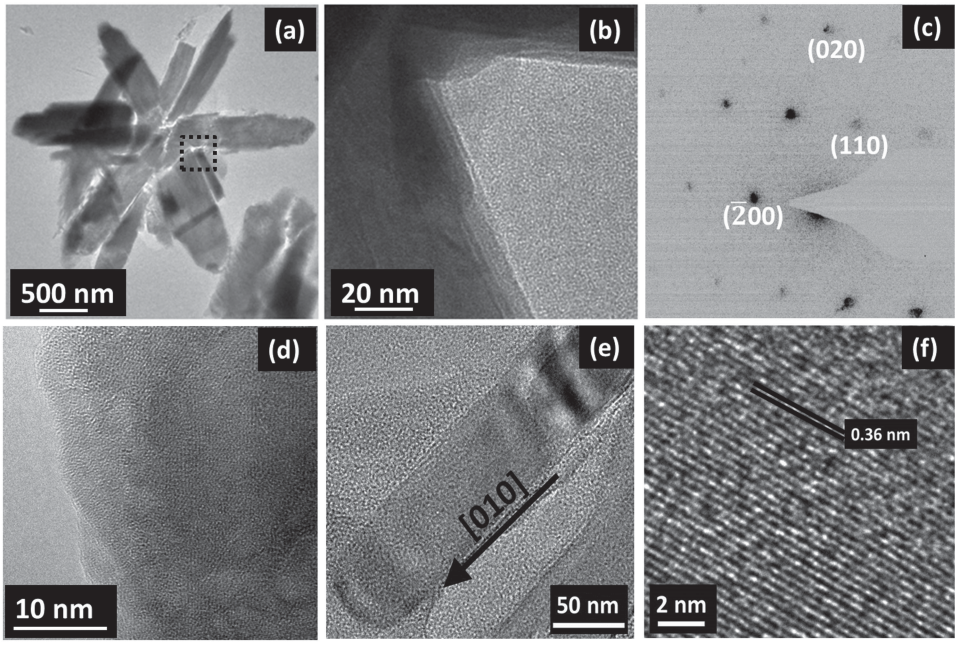

Figure 3. a) TEM image of a cross-sectioned VO_2(B) star-assembly; b) magnified image of arm intersection; c) corresponding indexed SAED pattern (on the (002) zone axis); d) magnified arm edge; e) overall and f) magnified view showing the [010] growth direction of the VO_2(B) nanobelts collected 4 h into the solvothermal growth process.

NANO MICRO small

along a crystallographic register; a SAED pattern for a mesocrystal is nearly identical to that of a single crystalline sample of the same material, making SAED a popular method for characterizing mesocrystals. Figure 3c displays the corresponding SAED pattern of the region from Figure 3b. The single crystal-like diffraction pattern is consistent with literature reports that index similar patterns as single crystalline VO_2(B).[30–32] Some distortion of the SAED pattern should be expected as the TEM image clearly shows that there are secondary particles present in addition to the arms of the cross sectioned star-structure being examined.

Figure 3d displays a magnified TEM image of a VO_2(B) star-assembly edge. The single crystalline nature of the VO_2(B) nanosheet is clearly visible as noted by the lattice fringes, and the dispersion of pores throughout the structure is also apparent. The preferred growth direction of the VO_2(B) structure is realized by considering the relative stacking rate of the octahedra at various crystal faces (Figure S1, Supporting Information). The shortest average bond in the VO_2(B) structure is along the [010] direction, which, based on the proposed formation mechanism, can account for the shape of the synthesized nanosheets and the overall architecture. Figure 3e,f depicts the growth direction of the VO_2(B) nanobelts collected before the solvothermal growth process was complete, where the lattice interspacing of 3.67 Å corresponds to the d_{010} spacing and the distance between two (010) crystallographic planes of the monoclinic structure; these findings corroborate that growth occurred along the [010] direction.[33] The establishment of the individual nanobelt and nanosheet growth directions, as viewed along the (002) zone axis, also reveals that the stacked nanosheets are oriented with one another along the [100] direction, and that the exposed surfaces of the nanosheets correspond to the (100) facet. Overall and lattice-resolution TEM imaging reveals that the individual VO_2(B) nanobelts and nanosheets exhibit preferential growth and stacking along the [010] and [100] directions, respectively, which is in agreement with previous literature results.[32]

The VO_2(B) nanostructures reported here were developed from the reduction of commercially available V_2O_5 utilizing additive-free solution-based processing methods as governed by the following reaction: $V_2O_5 + H_2C_2O_4 \rightarrow VO_2(B) + H_2O + CO_2$, where oxalic acid served as both the reducing and chelating agents because of its disposition to serve as a bidentate ligand. The precursor vanadium oxalate is synthesized as an intermediate during the reaction, as the conjugate base of oxalic acid, oxalate, is an excellent ligand for metal ions and usually binds forming a five-membered MO_2C_2 ring. The presence of the chelating agent should modify the surfaces of the growing nanocrystals, particularly the surfaces that possess the lowest electronic density, thus leading to the growth of specific surfaces and aiding in the synthesis of the observed micro-architectured nanosheet morphology.[34,35] The effects of solvothermal treatment time and oxalic acid concentration on the final superstructure are shown in Figure S2, Supporting Information.

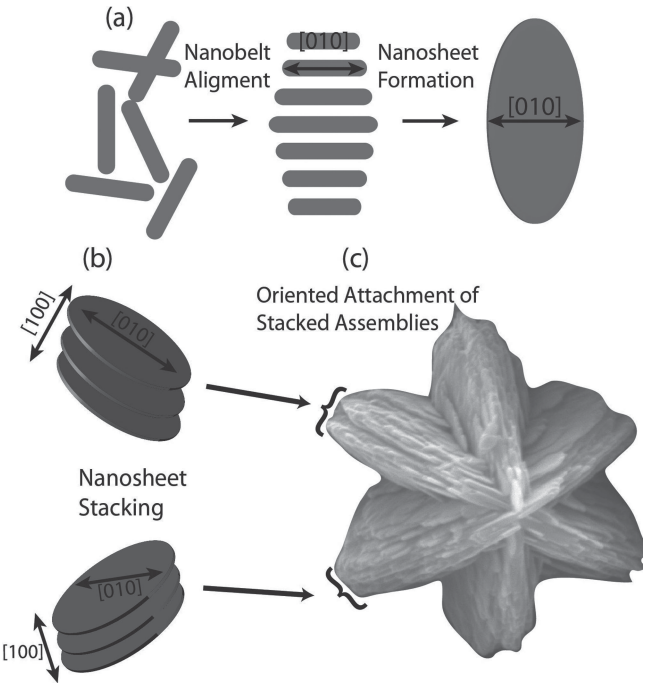

Figure 4. Proposed formation mechanism of the VO_2(B) mesocrystals: a) VO_2(B) nanobelts transform into VO_2(B) ellipsoidal nanosheets through Ostwald ripening where the semi-major axis of the nanosheet runs along the [010] crystallographic direction; b) several nanosheets stack on top of one another along the [100] direction (normal to the nanosheet surface) while residual chelating agent on the surface prevents fusion; c) series of stacked VO_2(B) nanosheets then form the star-like architecture through the oriented attachment mechanism.

Although the exact formation mechanism is not entirely clear, a schematic of the mesocrystal formation mechanism is proposed and illustrated in **Figure 4**, and supported with time resolved SEM growth images (Figure S3, Supporting Information). Figure 4a starts off with the VO_2(B) nanobelts that were directly observed 4 h into the solvothermal treatment. The nanobelts in solution will coarsen and grow into ellipsoidal VO_2(B) nanosheets through Ostwald ripening. The [010] growth direction of the VO_2(B) nanobelts is maintained during this step, as determined from SAED.[24,28,32]

Several nanosheets then stack homoepitaxially over one another in order to minimize the energy of the system. Residual chelating agent remaining on the (100) surface of each nanosheet effectively decreases the Debye length of the electric double layer and stabilizes the van der Waals forces of the constituting components, leading to superstructure formation while preventing fusion between individual nanosheets (Figure 4b).[19] Following this step, several series of stacked VO_2(B) nanosheets will coalesce together to form the star-like architecture through the oriented attachment mechanism, as depicted in Figure 4c.[36] There may be some degree of subsequent coarsening after the process is complete, but fusion of the individual VO_2(B) nanosheets should be circumvented due to the presence of the oxalic acid derived chelating agent.

Figure 5 presents the cyclic voltammetry (CV), variable rate discharge, cyclic stability curves, and comparison of the

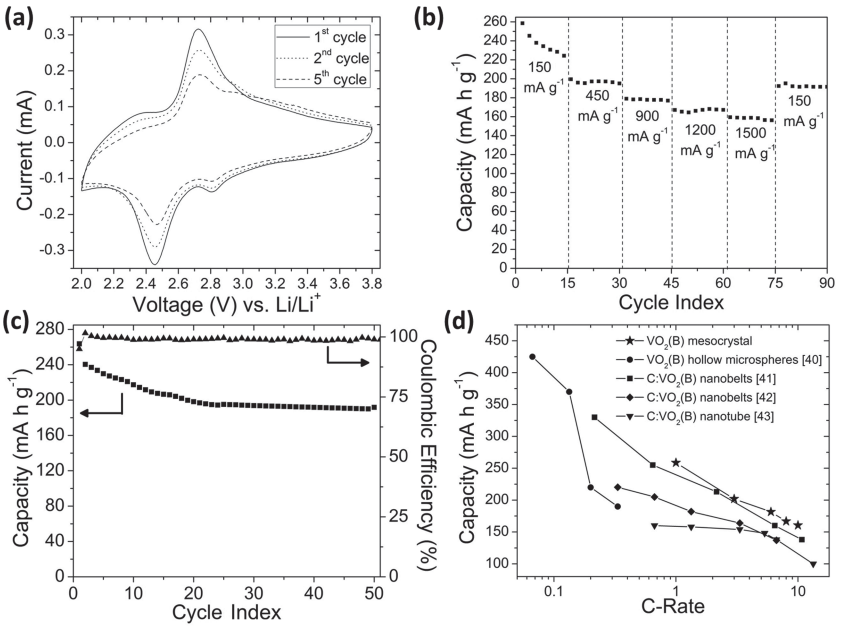

Figure 5. a) CV curves obtained at a scan rate of 0.5 mV s^{-1} for the 1st, 2nd, and 5th cycles; b) discharge-rate capability at various current densities; c) cycle stability and Coulombic efficiency over 50 cycles at 150 mA g^{-1}; and d) comparison with various VO-$_2$(B) structures from literature (assuming a 1C current density of 150 mA g^{-1}).

VO_2(B) mesocrystal electrodes with nanoparticle counterparts. Figure 5a depicts the first, second, and fifth CV curves collected at a scan rate of 0.5 mV s^{-1}. The cathodic and anodic peaks are located at 2.45 and 2.72 V versus Li/Li^+, and correspond, respectively, to the insertion and extraction of Li^+ into and out of the VO_2(B) structure. The diminishing peaks of the CV curve with cycling suggest that the star-assemblies are experiencing some degree of amorphization due to the incorporation of lithium upon cycling, but also reaffirm that that the as-obtained VO_2(B) mesocrystals can reversibly intercalate lithium.

It has been demonstrated, at least for the case of TiO_2, that the exposure of specific high-energy facets can increase the Li-ion intercalation capability due to unique surface properties. The charge transfer and chemical diffusion coefficient for TiO_2 is greatest along the (001) facet, and exposure of these facets can result in a lower energy barrier for faster and more efficient Li-ion intercalation.[37,38] Additionally, the TiO_2(B) (100) facet, with and without taking into account surface relaxation effects, has the greatest surface energy amongst the low-index surfaces;[39] this finding is of great significance given that the crystal structures of TiO_2(B) and VO_2(B) are analogous. Therefore, a similar mechanism may be at play for the case of VO_2(B) mesocrystals, where the exposed (100) facets at the surfaces of the nanosheets effectively enhances the Li-ion intercalation performance. This mechanism was investigated by qualitatively comparing the surface energies of specific facets by calculating the dangling (or broken) bonds per surface area upon cleaving particular lattice planes; relaxation effects after cleaving were not considered (Figure S4, Supporting Information). Using this method, it was determined that the (100) facet has a relatively high surface energy compared to the other primary facets, that is, (010), (110), (011), and (001), which corroborates the findings of Vittadini et al. for their analysis of TiO_2(B).[39] Of the considered facets, only the (101) facet had a larger qualitative surface energy. Thus, the exposure of the (100) facets should enhance the Li-ion intercalation performance of the VO_2(B) mesocrystalline star-assemblies.

The rate capability of the VO_2(B) mesocrystals when tested at incremental discharge rates for 15 cycles starting at 150 mA g^{-1} and terminating at 1500 mA g^{-1} is demonstrated in Figure 5b. The initial capacity was 258 mA h g^{-1}, but steadily dropped to 225 mA h g^{-1} after 15 cycles. The subsequent discharge tests showed reasonably stable capacity profiles of approximately 196, 177, 166, and 158 mA h g^{-1} over the course of 15 cycles at discharge rates of 450, 900, 1200, and 1500 mA g^{-1}, respectively. The exceptional discharge capacities can be attributed to the mesocrystalline structure that promotes electrolyte penetration, thereby increasing the contact area between the electrolyte and the electrode itself. Such traits, along with the oriented nanosheet structure, lead to great enhancement in the lithium-ion diffusivity, and the overall capacity.

The discharge rate was returned to 150 mA g^{-1} after the tests at higher discharge were completed, and was accompanied by a moderate drop from the initial capacity to approximately 195 mA h g^{-1}. The drop in capacity following cycling at higher discharge rates can be realized by examining the cycle stability test performed at 150 mA g^{-1} (Figure 5c). The initial capacity is equivalent to what was seen in the rate capability data, approximately 258 mA h g^{-1}. The capacity then drops with each cycle until reaching the 20th cycle, at which point the capacity appears to level off at approximately 195 mA h g^{-1}. These results indicate that there may be a slight degree of pulverization or solid state amorphization occurring in the VO_2(B) mesocrystals during the preliminary cycles due to the incorporation of lithium into the system, but an equilibrium is quickly established and then maintained. Figure 5d compares the mesocrystal intercalation performance with that of other VO_2(B) structures taken from the literature.[40–43] It should be noted that the conductive additive loadings in these studies were all equal to or greater than the amount of conductive additive used in this work. Despite their overall micro-scale size, the mesocrystals exhibit one of the highest intercalation performance and capacity retention, especially upon cycling at higher discharge rates. The excellent cycle stability can be attributed to the crystallographically oriented nanosheets that provide sufficient accommodation of lithium upon cycling, assuring that good electrochemical stability and mechanical integrity can be guaranteed for many cycles.

NANO MICRO small

3. Conclusion

An additive and template-free solvothermal process was developed for the facile synthesis of mesocrystalline VO_2(B). The VO_2(B) mesocrystals were proposed to form through the combination of classical as well as non-classical crystallization mechanisms. The synthesized VO_2(B) mesocrystals showed excellent cycle stability and high rate discharge when tested as positive electrode material for lithium-ion battery. The stacking of the nanosheets along high energy exposed facets can surpass capacity values for comparative nanostructures and the presence of pores throughout the material can better accommodate cycling induced strain, thus improving the cycle stability. Moreover, these results reveal that mesocrystals of functional materials with high crystallinity, high porosity, and nanoparticle alignment are promising candidates for potential energy storage applications.

4. Experimental Section

Materials and Synthesis: VO_2(B) mesocrystals were synthesized by adopting the methods of Li et al.[24] In a typical reaction, 25 mmol of V_2O_5 (Alfa Aesar) was combined with 15 mL of 0.1 M oxalic acid (Sigma-Aldrich) and stirred for 18 h. The oxalic acid served as the reducing and chelating agent. Completion of the reaction was noted by the color of the solution transitioning from yellow to blue, signifying a reduction of the vanadium species. The solution was then transferred into a polytetrafluoroethylene (PTFE) lined, 25 mL capacity stainless steel autoclave. The solvothermal reaction was carried out at 180 °C for 12 h, after which the final product was isolated and dried at 80 °C overnight.

Structural Characterization: The phase and crystallite size of the VO_2(B) mesocrystal material was studied using X-ray diffraction (XRD, Bruker X-ray diffractometer); the sample was scanned with Cu-K_α radiation within the range of 10° to 70° (2θ) using a step size of 0.02° and an exposure time of 10 s. The accelerating voltage and current were 40 kV and 40 mA, respectively. The surface morphology of the VO_2(B) mesocrystals was examined using scanning electron microscopy (SEM, JEOL JSM-7000F). The specific surface area and pore size distribution were determined from nitrogen sorption isotherms collected at 77 K using the Brunauer-Emmett-Teller (BET) and Barrett–Joyner–Halenda (BJH) desorption analyses, respectively (Quantachrome NOVA 4200e). Transmission electron microscopy (TEM) and selected-area electron diffraction (SAED) studies were carried out using an aberration-corrected Titan 80–300 scanning/transmission electron microscope (S/TEM) operating at 80 kV after the sample had been embedded in Araldite 502 (SPI-Chem) epoxy resin and then cut to 100 nm thick segments with using a Leica EM UC6 ultramicrotome.

Electrochemical Measurements: The electrode slurry was prepared by mixing the as-synthesized VO_2(B), Super P conductive carbon (TIMCAL Graphite & Carbon), and poly(vinylidene fluoride) (PVDF, Sigma-Aldrich) binder dispersed in a N-methyl-2-pyrrolidone (NMP, Alfa Aesar) solution at a weight ratio of 80:12:08, respectively. The slurry was spread onto aluminum foil and dried in an oven at 80 °C overnight prior to coin-cell assembly. The 2032-type half-cells were assembled in an argon filled glove box (MTI, Corp.). A polypropylene membrane (Celgard 2400) was used as the separator, Li-metal as the counter and reference electrodes, and 1 M $LiPF_6$ in ethylene carbonate/dimethyl carbonate (1:1, v/v ratio) as electrolyte. Cyclic voltammograms (CVs) were collected using an electrochemical analyzer (CH Instruments, Model 605B) in the voltage range of 2.0–3.8 V (vs Li/Li^+). The Li-ion cycle stability and rate performance of the VO_2(B) mesocrystals was evaluated using an Arbin Battery Tester BT-2000 (Arbin Instruments, College Station, TX) operating at room temperature. The half-cells were tested within a voltage cut-off range of 2.0–3.8 V versus Li/Li^+ at various current rates; the capacity values were based on the weight of the electro-active material alone.

Supporting Information

Supporting Information is available from the Wiley Online Library or from the author.

Acknowledgements

This research work has been financially supported in part by the National Science Foundation (NSF, CMMI-1030048) and the University of Washington TGIF grant. Part of this work was supported by the Laboratory Directed Research and Development (LDRD) program of Pacific Northwest National Laboratory (PNNL). Part of this work was conducted in the William R. Wiley Environmental Molecular Sciences Laboratory (EMSL), a national scientific user facility sponsored by DOE's Office of Biological and Environmental Research and located at PNNL. E.U. would like to acknowledge financial support from The Boeing Company.

[1] Y.-G. Guo, J.-S. Hu, L.-J. Wan, *Adv. Mater.* **2008**, *20*, 2878.
[2] L. Shen, H. Li, E. Uchaker, X. Zhang, G. Cao, *Nano Lett.* **2012**, *12*, 5673.
[3] L. Shen, E. Uchaker, X. Zhang, G. Cao, *Adv. Mater.* **2012**, *24*, 6502.
[4] E. Uchaker, N. Zhou, Y. Li, G. Cao, *J. Phys. Chem. C* **2013**, *117*, 1621.
[5] M. Wagemaker, F. M. Mulder, A. Van der Ven, *Adv. Mater.* **2009**, *21*, 2703.
[6] M. N. Ou, S. R. Harutyunyan, S. J. Lai, C. D. Chen, T. J. Yang, Y. Y. Chen, *Phys. Status Solidi B* **2007**, *244*, 4512.
[7] B. V. Ratnakumar, M. C. S. S. Surampudi, *J. Power Sources* **2001**, *97*, 137.
[8] M. Jo, Y.-S. Hong, J. Choo, J. Cho, *J. Electrochem. Soc.* **2009**, *156*, A430.
[9] H. Dong, Y. J. S. Jang, Seung M. Oh, *J. Electrochem. Soc.* **1996**, *143*, 2204.
[10] Q. F. Zhang, E. Uchaker, S. L. Candelaria, G. Z. Cao, *Chem. Soc. Rev.* **2013**, *42*, 3127.
[11] A. Nel, T. Xia, L. Madler, N. Li, *Science* **2006**, *311*, 622.
[12] V. L. Colvin, *Nat. Biotechnol.* **2003**, *21*, 1166.
[13] H. Colfen, M. Antonietti, *Angew. Chem. Int. Ed.* **2005**, *44*, 5576.
[14] R.-Q. Song, H. Coelfen, *Adv. Mater.* **2010**, *22*, 1301.
[15] R.-Q. Song, H. Coelfen, *CrystEngComm* **2011**, *13*, 1249.
[16] M. Antonietti, G. A. Ozin, *Chem. Eur. J.* **2004**, *10*, 28.
[17] F. C. Meldrum, H. Coelfen, *Chem. Rev.* **2008**, *108*, 4332.

[18] R. O. Da Silva, R. H. Goncalves, D. G. Stroppa, A. J. Ramirez, E. R. Leite, *Nanoscale* **2011**, *3*, 1910.
[19] C. Lausser, H. Coelfen, M. Antonietti, *ACS Nano* **2011**, *5*, 107.
[20] J. Popovic, R. Demir-Cakan, J. Tornow, M. Morcrette, D. S. Su, R. Schloegl, M. Antonietti, M.-M. Titirici, *Small* **2011**, *7*, 1127.
[21] J. Ye, W. Liu, J. Cai, S. Chen, X. Zhao, H. Zhou, L. Qi, *J. Am. Chem. Soc.* **2011**, *133*, 933.
[22] A. Baynton, T. Radomirovic, M. I. Ogden, C. L. Raston, W. R. Richmond, F. Jones, *CrysteEngComm* **2011**, *13*, 109.
[23] S. Mann, *Nat. Mater.* **2009**, *8*, 781.
[24] G. Li, K. Chao, H. Peng, K. Chen, Z. Zhang, *Inorg. Chem.* **2007**, *46*, 5787.
[25] G. Armstrong, J. Canales, A. R. Armstrong, P. G. Bruce, *J. Power Sources* **2008**, *178*, 723.
[26] A. M. Kannan, A. Manthiram, *Solid State Ion.* **2003**, *159*, 265.
[27] H. Yin, K. Yu, Z. Zhang, Z. Zhu, *Appl. Surf. Sci.* **2011**, *257*, 8840.
[28] G. Li, K. Chao, C. Zhang, Q. Zhang, H. Peng, K. Chen, *Inorg. Chem.* **2009**, *48*, 1168.
[29] L. Zhou, P. O'Brien, *J. Phys. Chem. Lett.* **2012**, *3*, 620.
[30] W. Jiang, J. Ni, K. Yu, Z. Zhu, *Appl. Surf. Sci.* **2011**, *257*, 3253.
[31] C. Leroux, G. Nihoul, G. Van Tendeloo, *Phys. Rev. B* **1998**, *57*, 5111.
[32] J. F. Liu, Q. H. Li, T. H. Wang, D. P. Yu, Y. D. Li, *Angew. Chem. Int. Ed.* **2004**, *43*, 5048.
[33] C. M. Julien, A. Mauger, K. Zaghib, *J. Mater. Chem.* **2011**, *21*, 9955.
[34] A. Pan, H. B. Wu, L. Yu, X. W. Lou, *Angew. Chem. Int. Ed.* **2013**, *52*, 2226.
[35] A. Pan, T. Zhu, H. B. Wu, X. W. Lou, *Chemistry* **2013**, *19*, 494.
[36] V. M. Yuwono, N. D. Burrows, J. A. Soltis, R. L. Penn, *J. Am. Chem. Soc.* **2010**, *132*, 2163.
[37] Y. Liu, E. Uchaker, N. Zhou, J. Li, Q. Zhang, G. Cao, *J. Mater. Chem.* **2012**, *22*, 24439.
[38] C. H. Sun, X. H. Yang, J. S. Chen, Z. Li, X. W. Lou, C. Li, S. C. Smith, G. Q. Lu, H. G. Yang, *Chem. Commun.* **2010**, *46*, 6129.
[39] A. Vittadini, M. Casarin, A. Selloni, *J. Phys. Chem. C* **2009**, 113, 18973.
[40] H. Liu, Y. Wang, K. Wang, E. Hosono, H. Zhou, *J. Mater. Chem.* **2009**, *19*, 2835.
[41] M. M. Rahman, J.-Z. Wang, N. H. Idris, Z. Chen, H. Liu, *Electrochim. Acta* **2010**, *56*, 693.
[42] Q. Zhao, L. Jiao, W. Peng, H. Gao, J. Yang, Q. Wang, H. Du, L. Li, Z. Qi, Y. Si, Y. Wang, H. Yuan, *J. Power Sources* **2012**, *199*, 350.
[43] X. Rui, D. Sim, C. Xu, W. Liu, H. Tan, K. Wong, H. H. Hng, T. M. Lim, Q. Yan, *RSC Advances* **2012**, *2*, 1174.

Received: December 19, 2012
Revised: February 4, 2013
Published online: May 5, 2013

